A pressure field reconstruction scheme based on velocity data for strong shock-wave/boundary-layer interactions with regular and Mach reflections

Liu, Shun; Chen, Jing; van Oudheusden, Bas W.; Xu, Jinglei; Schrijer, Ferry F.J.; Gao, Bo

Important note
To cite this publication, please use the final published version (if applicable).
Please check the document version above.

A pressure field reconstruction scheme based on velocity data for strong shock-wave/boundary-layer interactions with regular and Mach reflections ⊘

Shun Liu (刘顺) ✉ iD ; Jing Chen (陈京); Bas W. van Oudheusden iD ; Jinglei Xu (徐惊雷) ✉ iD ;
Ferry F. J. Schrijer iD ; Bo Gao (高波) iD

Check for updates

View Online   Export Citation

Physics of Fluids

AIP Publishing

Physics of Fluids

Special Topics Open for Submissions

Learn More

A pressure field reconstruction scheme based on velocity data for strong shock-wave/ boundary-layer interactions with regular and Mach reflections

Shun Liu (刘顺),[1,2,a] (iD) Jing Chen (陈京),[1] Bas W. van Oudheusden,[3] (iD) Jinglei Xu (徐惊雷),[4,a] (iD) Ferry F. J. Schrijer,[3] (iD) and Bo Gao (高波)[1] (iD)

AFFILIATIONS

[1]School of Energy and Power Engineering, Jiangsu University, Zhenjiang 212013, China
[2]Laboratory of Aerodynamic Noise Control, China Aerodynamics Research and Development Center, Mianyang 621000, China
[3]Faculty of Aerospace Engineering, Delft University of Technology, Kluyverweg 1, Delft 2629 HS, the Netherlands
[4]College of Energy and Power Engineering, Nanjing University of Aeronautics and Astronautics, Nanjing 210016, China

[a]Authors to whom correspondence should be addressed: liushun@ujs.edu.cn and xujl@nuaa.edu.cn

ABSTRACT

In this paper, a non-intrusive pressure measurement scheme based on particle image velocimetry (PIV) is presented for the complex supersonic flows with intense shock systems, by elaborately combining the MacCormack method, the streamline-based method, and the spatial integration in conservative form. According to the detailed analyses of flow structures, the pressure fields are well reconstructed by the proposed scheme for the two typical shock-wave/boundary-layer interactions containing regular and Mach reflections, which are induced by the relatively strong oblique shock waves generated by the wedges of 21° and 17° in the freestreams of Mach 2.5 and 2.0, respectively. Based on the theoretical solutions by oblique shock relationship, free interaction theory, and shock polar analysis, this pressure reconstruction scheme is completely validated to effectively suppress the propagation of PIV velocity error to the pressure field and the accumulation of reconstructed pressure error behind the strong shock wave. Compared with the literature presently, this work would be the most challenging application of PIV-based pressure measurement to such complex supersonic flows with intense shock reflections, large oscillations, wide speed ranges, and various compressible flow structures. These good results could confirm the feasibility and high accuracy of the proposed reconstruction scheme and may greatly promote its applications in academic research and engineering test for supersonic flows in the future.

Published under an exclusive license by AIP Publishing. https://doi.org/10.1063/5.0249869

I. INTRODUCTION

Particle image velocimetry (PIV), as a non-intrusive and quantitative velocity measurement technique with high spatial resolution inside flow field, plays an important role in experimental fluid dynamics. Compared with the intrusive measurement equipment such as pressure probe and hot-wire anemometer, PIV captures the motion of tracer particle with good flow-following ability to obtain velocity field without interference with original flow, which shows significant advantage in the measurement of supersonic flow containing complex shock/compression/expansion waves and boundary/shear layers.[1] In addition, PIV could record the quantitative velocity information of entire flow field with high spatial resolution simultaneously, which is more beneficial to the evaluation of flow structure than the single-point measurement of laser Doppler velocimetry and the qualitative measurement of schlieren.

In addition to the velocity field directly measured by PIV, the quantitative visualization of pressure field is also of great guiding significance for flow mechanism analysis and aerodynamic performance estimation, especially in the internal flow of aero-engine[2–4] and the external flow of aircraft.[5–7] However, there are many problems in the application of traditional pressure measurement equipment to supersonic flows. The conventional pressure probe placed inside flow field would seriously perturb the original flow structure, leading to the obvious deterioration of measurement accuracy especially in complex supersonic flows. The advanced non-intrusive pressure sensitive paint could only measure the pressure distribution on the surface but is not

applicable inside flow. Therefore, in the past 20 years, a PIV-based pressure reconstruction measurement technique showed great attractions and had become an important quantitative visualization method in experiments of fluids.[8] The fundamental theory is to establish the relationship between velocity and pressure fields according to Navier–Stokes (N–S) equations, and then, specific numerical methods could be applied to reconstruct the pressure distribution based on the velocity data measured by PIV.

In the early stage, the research on PIV-based pressure measurement focused on incompressible flows. In 1999, Baur[9] and Gurka et al.,[10] respectively, proposed the two most popular methods of pressure reconstruction, called the spatial integration (SI) method and the Poisson equation-based method, which quickly received great attention in the optical flow measurement. The basic principle is to separate the pressure term from the other terms in the momentum equation and then substitute the velocity terms by PIV velocity data to obtain the pressure gradient distribution of the flow field:[9]

$$\nabla p = -\rho \frac{D\mathbf{u}}{Dt} + \mu \nabla^2 \mathbf{u}, \tag{1}$$

where $\mathbf{u}$ and t represent velocity vector and time. The density ρ and dynamic viscosity μ can be regarded as known constants in incompressible flows, and the acceleration $D\mathbf{u}/Dt$ is calculated by Lagrangian or Eulerian methods.[11] Then, the spatial integration could be conducted based on the prescribed Dirichlet boundary condition to achieve the pressure distribution of the entire flow field. The Poisson method is to further rewrite Eq. (1) into the form of the Poisson equation:[10]

$$\nabla^2 p = \nabla \cdot \left(-\rho \frac{D\mathbf{u}}{Dt} + \mu \nabla^2 \mathbf{u}\right) = -\rho \nabla \cdot (\mathbf{u} \cdot \nabla)\mathbf{u} \tag{2}$$

and then solve the pressure field by adopting standard numerical methods in mathematics such as the successive over relaxation[10] and the spectral method.[12] However, for a long period afterward, the research on PIV-based pressure reconstruction mainly focused on improving the accuracy of numerical algorithms,[13–16] optimizing the integration path,[17–19] and experimental applications[20–22] in incompressible flows, but without substantial breakthrough.

Until 2007, the first significant breakthrough of PIV-based pressure measurement was made by van Oudheusden[23] to achieve the basic principle for compressible flows, which can be regarded as a developmental milestone. The greatest difficulty in compressible flow lies in the extra unknown variable of density. Therefore, various equations and numerical methods should be adopted based on different flow conditions and assumptions.[8] In the high subsonic flow, most of the field far from the boundary layer, shear layer, and wake belongs to the isentropic flow region, where exists a clear algebraic relation between velocity and pressure:[24]

$$\frac{p}{p_\infty} = \left(1 + \frac{\gamma - 1}{2} M_\infty^2 \left(1 - \frac{V^2}{V_\infty^2}\right)\right)^{\frac{\gamma}{\gamma-1}}, \tag{3}$$

where, γ, V, and M are the specific heat ratio, velocity magnitude, and Mach number, and the subscript ∞ represents the freestream. Apparently, Eq. (3) no longer holds for non-isentropic regions, where additional equations need to be introduced to deal with the density

term. The general operation is to first obtain the distribution of temperature T by assuming the adiabatic flow condition

$$\frac{T}{T_\infty} = 1 + \frac{\gamma - 1}{2} M_\infty^2 \left(1 - \frac{V^2}{V_\infty^2}\right). \tag{4}$$

This assumption is reasonable in most of the wind tunnel experiments without severe heat transfer.[25] Then, the pressure gradient and the velocity can be decoupled by replacing the density in Eq. (1) with the pressure and temperature according to the ideal gas equation of state, while the viscous term is ignored reasonably.[8,23] Finally, the basic principle of PIV-based pressure reconstruction for the high subsonic flow is achieved as follows::[23]

$$\frac{\nabla p}{p} = \nabla \ln(p/p_\infty) = -\frac{1}{RT} \cdot \frac{D\mathbf{u}}{Dt}$$
$$= -\left(\frac{\gamma M_\infty^2}{V_\infty^2 + \frac{\gamma-1}{2} M_\infty^2 (V_\infty^2 - V^2)}\right) \cdot \frac{D\mathbf{u}}{Dt}, \tag{5}$$

where R represents the gas constant. Based on Eq. (5), the classic SI method and the Poisson method are also applicable to reconstruct the pressure field. Ragni et al.[26–28] successfully obtained the wake pressure field of NACA 0012 airfoil in Mach 0.6 freestream by the SI method and the transonic (Mach 0.7) pressure field near the blade-tip of an aircraft propeller by the Poisson method. In addition, van Gent et al.[29–32] conducted a series of validation, evaluation, and application of the pressure field reconstruction for a scaled rocket wake flow in Mach 0.7 freestream. These results highlight the inherent advantages of non-intrusion, high spatial resolution, and full field measurement about the PIV-based pressure reconstruction technique.

However, in supersonic flows, the accuracy of reconstructed pressure field behind shock wave (as flow discontinuity) deteriorates seriously because Eq. (5) is derived from the inviscid momentum equation in non-conservative form, without explicitly introducing the physical constraint of flow conservation.[33] To solve this problem, the initial scheme is to determine the shock wave position based on the divergence of velocity field and then use the theoretical shock relation to accurately propagate the pressure information across the shock wave.[23] However, this is quite difficult to implement in the supersonic flow with complex shock wave system, while the reconstruction error is highly sensitive to the accuracy of shock position, thus increasing the uncertainty of reconstructed pressure field.[23] In 2008, van Oudheusden et al.[33] made another important breakthrough to first propose a novel pressure reconstruction method, especially for the steady/time-averaged supersonic flow containing complex shock wave system. The basic equation is achieved by using the conservative form of the momentum equation combined with the adiabatic assumption of Eq. (4). The Einstein summation is adopted for the more concise formulation

$$\left(\delta_{ij} + \frac{u_i u_j}{RT}\right) \frac{\partial \ln(p/p_\infty)}{\partial x_j} = -\frac{1}{RT} \left(\frac{\partial u_i u_j}{\partial x_j} - \frac{u_i u_j}{T} \frac{\partial T}{\partial x_j}\right), \tag{6}$$

where u_i and u_j are velocity components and δ_{ij} denotes the Kronecker symbol. Equation (6) shows better numerical stability across shock wave due to the inherent flow continuity constraint in the conservative momentum equation,[34] allowing to reconstruct the correct pressure

field downstream without the special treatment to shock wave.[33] The spatial integration based on Eq. (6) is called the conservative SI (CSI) method, which had been verified by using the shock-wave/boundary-layer interaction (SWBLI) induced by a wedge model of 8° in Mach 2.07 freestream and the flow around a bi-convex airfoil in Mach 1.96 freestream.[33] The pressure ratios across the shock waves in the two cases do not exceed 2 because of relatively weak shock intensity. Afterward, the research on PIV-based pressure measurement for supersonic flow almost kept stagnant during the following decade.

In recent years, with the great development of supersonic aircraft, the technique of PIV-based pressure reconstruction measurement received more attention again due to its unique advantages of non-intrusion and high spatial resolution. The increasing design Mach number of modern supersonic aircraft results in a significant enhancement of shock intensity as well as flow discontinuity in the wind tunnel experiment, leading to the severe deterioration of reconstructed pressure field obtained by spatial integration or Poisson solver based on Eq. (6).[35] Therefore, since 2017, Liu *et al.*[35–40] have made a series of research types on pressure reconstruction algorithm and its experimental application in supersonic flows with relatively strong shock waves, which could be regarded as another major breakthrough in PIV-based pressure measurement. From 2017 to 2019, the MacCormack method was proposed especially for overcoming the serious accumulation of pressure reconstruction error behind strong shock wave, and fully validated by numerical and experimental data.[35–37] In addition, the failure reason for the CSI and Poisson methods in strong shock flows was elaborated from the perspectives of physics and mathematics.[35] In 2020, Liu *et al.*[38] further proposed a streamline-based (SLB) reconstruction method according to the continuity equation in integral form, which reduces the consumption of computing resource and the careful consideration of numerical stability in the MacCormack method. Afterward, these methods were applied to the internal flows of supersonic inlet and single expansion ramp nozzle for aerodynamic performance measurement.[39,40] However, these applications still remained in theoretical evaluations based on numerical velocity fields but without experimental validations.

In fact, although these reconstruction methods proposed for supersonic flow have been verified by the experimental data of single intense oblique or bow shock wave, it is still quite challenging to apply them properly to an unknown complex supersonic flow. First, the relatively strong wave system poses a great challenge to the velocity measurement accuracy of PIV itself.[41] Thus, it is a critical problem to suppress the propagation of the large velocity error to the reconstructed pressure field. Second, different pressure reconstruction methods show their best performance in specific flow structures and velocity ranges. Therefore, it is important to couple various methods properly to achieve the highest reconstruction accuracy in complex supersonic flow. Finally, compared with the wide recognition of PIV-based pressure measurement in low-speed flows, there are a few practical applications in supersonic flows with intense shock systems at present, although the appropriate methods have been proposed for several years. As a result, a convincible application with detailed accuracy evaluation to a typical complex supersonic flow is much-needed and may greatly promote the development of this technique.

SWBLI is the most common supersonic flow in high-speed aircraft and propulsion system.[42] It includes all typical compressible flow structures such as shock/compression/expansion waves and complex reflections with boundary layer/separation bubble, which could be the best selection for evaluating the PIV-based pressure reconstruction scheme in supersonic flow. This paper conducts two sets of PIV measurements of strong SWBLIs containing regular and Mach reflections, induced by 21°/17° wedge models in the freestreams of Mach 2.5/2.0, respectively. Then, the reconstruction coupling scheme is established by properly adopting the MacCormack method, the SLB method, and the CSI method, based on the detailed analyses of flow structures measured by PIV. Finally, the reconstructed pressure fields are comprehensively evaluated by the comparisons with the theoretical solutions of the oblique shock relationship, the free interaction theory, and the shock polar analysis, which fully verifies the feasibility, stability, and high accuracy of the proposed PIV-based pressure reconstruction scheme for complex supersonic flows in academic research types and engineering tests.

II. EXPERIMENTAL SETUP

This section introduces the supersonic wind tunnel, the experimental models (shock generators), and the measurement equipment (PIV and schlieren) for conducting the measurements of two strong SWBLIs induced by the wedge models of 21°/17° in the freestream of Mach 2.5/2.0, containing the regular/Mach reflections. In addition, the particle relaxation is evaluated by the incident oblique shock generated by the 21° wedge, demonstrating the reliability of the PIV setup in the SWBLIs.

A. Wind tunnel and model

The two sets of experiments are carried out in the supersonic blowdown wind tunnel ST-15 shown in Fig. 1(a) at Delft University of Technology. The inlet is connected with the dried air source with a total pressure/temperature of 3 bar/302 K. By replacing the fixed nozzles, the freestream can achieve nominal Mach 2.5 and 2.0. The test sections are designed to be integrated with the nozzle walls, with a same span width of 150 mm and different heights of 150/160 mm (Mach 2.5/2.0). Circular optical windows with a diameter of 250 mm are installed on the two sides of the test section for the measurements of PIV and schlieren, as shown in Fig. 1(b).

Figure 1(c) shows the shock generators with a span width of 120 mm, resulting in a distance of 15 mm away from the sidewall to prevent damage to the optical glass, which may increase the optical distortion in PIV and schlieren images. The length of the wedge models is 150 mm, and the thickness reaches the maximum 20 mm at the inflection point and then gradually decreases to 10 mm at the trailing edge, for reducing the effect of the expansion wave fan on the main structures of the SWBLI. The models are fixed on the upper wall of the test section by a bracket shown in Fig. 1(b). The heights from the leading edge to the lower wall are 100 mm (21°) and 128 mm (17°).

In fact, the inlet Mach number of the test section is slightly lower than the nominal value due to the boundary layer and the small step on the wind tunnel wall. According to the incident shock angle and the flow deflection angle measured by PIV and schlieren, it can be derived that the real Mach numbers (velocities) of the freestreams are 2.42 (572 m/s) and 1.98 (516 m/s) in the two sets of experiments. The detailed analyses can be found in Sec. III B. The parameters of boundary layer, including 99% thickness δ, friction velocity u_τ, skin friction coefficients cf, and Reynolds number Re_δ, will be elaborately evaluated in Sec. III A. The flow conditions are summarized in Table I, where
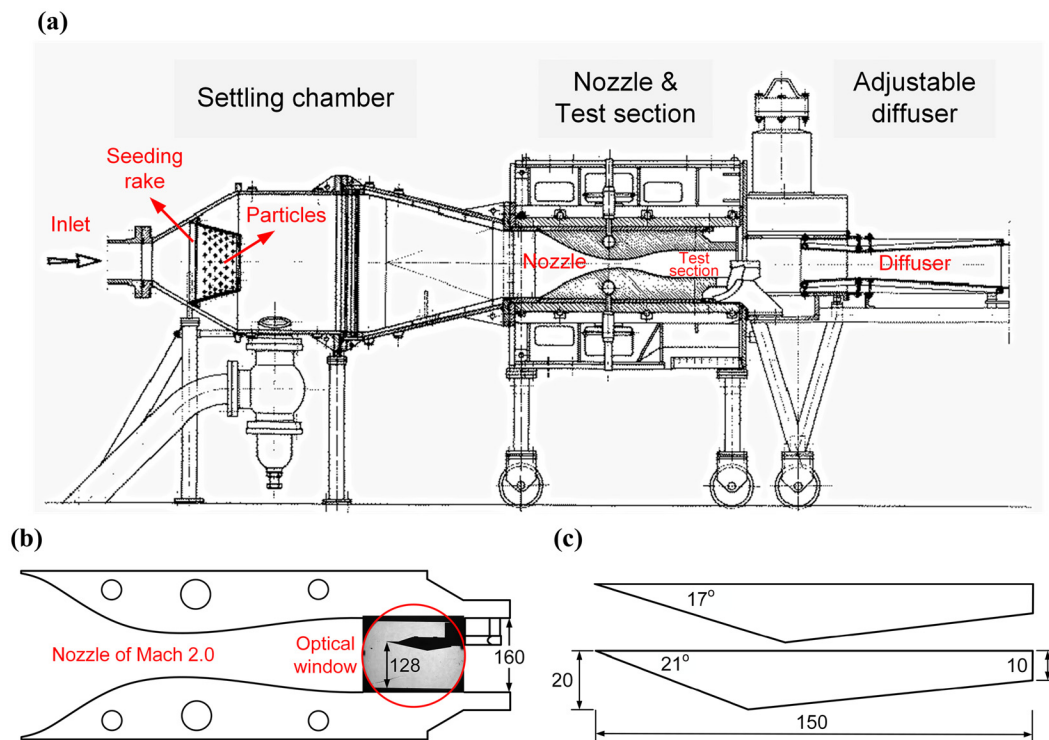
FIG. 1. Wind tunnel and model. (a) ST-15 wind tunnel. (b) Model installation. (c) Wedge model.

EXP 1 and 2 denote the experiments in the freestreams of nominal Mach 2.5/2.0, respectively.

B. PIV and schlieren equipment

The maximum frequency of general time-resolved PIV is on the order of 10 kHz,[43] which is still not enough to capture the continuous time-resolved data for the SWBLI.[44] Therefore, a low-speed PIV system is adopted here because the shorter pulse width of low-frequency laser is more beneficial for reducing the motion blur of the high speed tracing particle. In addition, this work mainly focuses on the nominal two-dimensional flow field in the middle span plane, and then, a planar PIV is sufficient for the present PIV measurements.

TABLE I. Flow conditions.

Parameter	Experimental cases	
	EXP 1	EXP 2
M_∞ (nominal/practical)	2.5/2.42	2.0/1.98
V_∞ (m/s)	572	516
P_0 (bar)	3	3
T_0 (K)	302	302
δ (mm)	5.55	5.32
u_τ (m/s)	22.9	19.3
c_f	1.54×10^{-3}	1.62×10^{-3}
Re_δ	8.9×10^{4}	1.25×10^{5}

The non-toxic di-ethyl-hexyl-sebacate (DEHS) is used for generating tracer particles by the PIVTec PIVpart 45 seeder which contains 45 Laskin nozzles and 1 impactor plate for removing oversized particles. At a pressure difference of 1 bar, the particles with a nominal diameter of 1 μm can be generated and uniformly sprayed into the settling chamber through a seeding rake with multiple small holes, as shown in Fig. 1(a). The particle relaxation time is about 2.0 μs, which is evaluated in Sec. II C and fully applicable to supersonic flows with shock waves.[42] The dual pulse Nd: YAG laser of Lumibird EverGreen is used for illuminating the field of view (FOV) with a frequency of 15 Hz and a wavelength of 532 nm. The maximum pulse energy is about 200 mJ and the pulse width is less than 10 ns. To obtain particle images with appropriate size and brightness, the pulse energy is set to 180 mJ in this experiment. The camera adopts LaVision Imager LX 2M, with a CCD resolution of 1623×1235 pixel^2 and a pixel size of 4.4×4.4 μm^2. It is equipped with Nikon lens with a focal length of 50 mm and an aperture $f_\#$ of 5.6. Based on these settings, the digital resolution of PIV images is about 47.5 μm/pixel, and the particle size is 2–3 pixels, which are beneficial for the cross-correlation in the post-processing, as shown in Fig. 2. The synchronous controller of LaVision PTU is used to set the pulse separation Δt to 2.3 μs, resulting in a particle displacement of about 1.32 mm (corresponding to a pixel displacement of about 27.7 pixels) in the freestream of Mach 2.5. In addition, the black matte paint is sprayed on the wedge model surface and the lower wall of the test section, to suppress the laser reflection. Each set of experiment is repeated 4 times to obtain 800 image pairs, which are enough to achieve the credible time-averaged and turbulent velocity data.
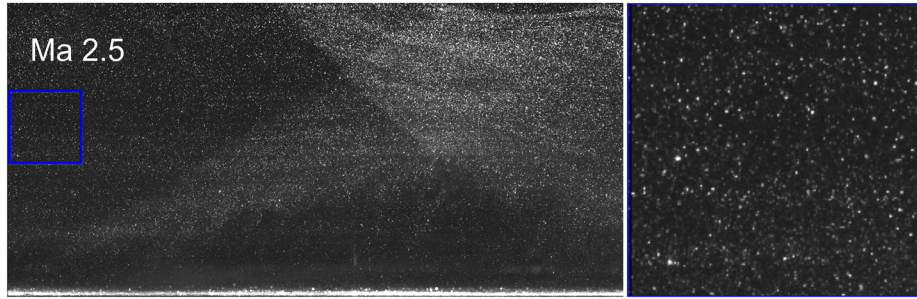
FIG. 2. Instantaneous particle image of SWBLI (Mach 2.5, regular reflection).

The schlieren system is also used for an auxiliary measurement with the aim of capturing the entire wave system in the test section. This is necessary for the accurate calibration of freestream Mach number and the arrangement of FOV in PIV measurement. The parallel light of schlieren can cover the entire optical window, as shown in Fig. 1(b), and the flow structures are captured by a high-speed camera of LaVision Imager HS with a frequency of 5 kHz and a resolution of 2016 × 2016 pixels. The sampling time is set to 2 s.

C. PIV arrangement and data processing

Figure 3 shows the PIV configuration and the FOVs. The laser beam reflected by a 45° mirror passes through a lens group to form a laser sheet, which enters the wind tunnel across a small optical window on the lower wall of the diffusion section. Then, the laser sheet is reflected by another 45° mirror to the test section, focusing in the FOV with a thickness of about 1.5 mm, as shown in Fig. 3. It should be noted that the windward area of the 45° mirror inside the tunnel is small and placed as close to the lower wall as possible, to prevent serious oscillation in the supersonic flow. This greatly limits the illumination area of FOV 1 with a maximum effective height of 38 mm and a width of 75 mm, as shown in Fig. 4(a). The typical features of the SWBLI with regular reflection are sufficient to be captured by the FOV 1, while the Mach reflection needs another FOV 2 combined with FOV 1 to achieve a larger field of 75 × 43 mm², as shown in Fig. 4(b). The velocity data in the overlapping part of the two FOVs are averaged.

Figures 2 and 5 show the original instantaneous particle images of the SWBLIs with regular and Mach reflections. It can be observed that the particle distribution is relatively uniform in the freestream,
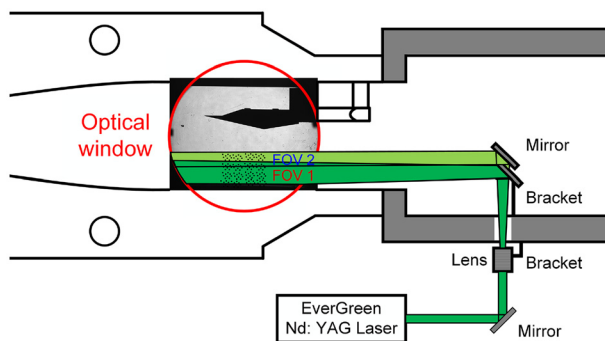

FIG. 3. PIV configuration and FOVs.

and the serious accumulation caused by particle relaxation appears after the shock waves. The particle concentration is low in the boundary layer and separation bubble. The laser reflection is suppressed by the blackened lower wall of the test section to some extent, but it still significantly affects the velocity measurement inside the boundary layer. In the Mach 2 experiment, an abnormal bright spot appears in the lower right corner of the particle image, as shown in Fig. 5. The reason is unknown, and therefore, a manual mask is adopted. In contract, the particle image of Fig. 2 in the Mach 2.5 experiment does not show similar bright spot. Overall, the original particle images with high quality demonstrate the proper arrangement of PIV system, and the typical flow structures of SWBLI are well captured.

The post-processing for the particle image pairs is performed by DaVis 8.2. First, the images are entirely rotated to compensate for the small angle between the camera and the lower wall of the test section. Then, a high pass filter of 5 × 5 pixels and a max/min filter are adopted to remove the background noise and normalize the light intensity, respectively. In addition, an automatic masking algorithm is used to quickly eliminate the low-quality part of each image pair. Furthermore, a total of 5 iterations are implemented by the window deformation iterative multi-grid (WiDIM) algorithm with a final interrogation window of 32 × 32 pixels and an overlap of 75%, resulting in a vector grid resolution of 0.38 mm. Finally, a median filter of 3 iterations is conducted for the original velocity field, and a smoothing filter is further used to improve the data quality. Table II summarizes the PIV recording and post-processing parameters.

D. Evaluation of particle relaxation

The velocity changes severely in supersonic flows with strong wave systems, and then, the PIV measurement uncertainty is mainly attributed to the relaxation effect of tracer particle,[42] including relaxation time τ_p and relaxation distance ξ_P:[1,45]

$$\tau_p = d_p^2 \frac{\rho_p}{18\mu_f}(1 + 2.7Kn_d),\tag{7}$$

$$\xi_p = \tau_p\left[u_{n1} - (u_{n1} - u_{n2}) \cdot e^{-1}\right],\tag{8}$$

where d_p and ρ_p denote the diameter and density of the agglomerated particle. μ_f is the viscosity coefficient of the fluid, and the Knudsen number kn_d represents the ratio of the average molecule free path to the particle diameter. However, the theoretical equations could only roughly provide a qualitative evaluation of relaxation characteristics, but cannot be used for the direct calculation of relaxation time and distance in real PIV experiment. The reasons are as follows:[46] (1) the particle agglomeration would be changed by the acceleration and
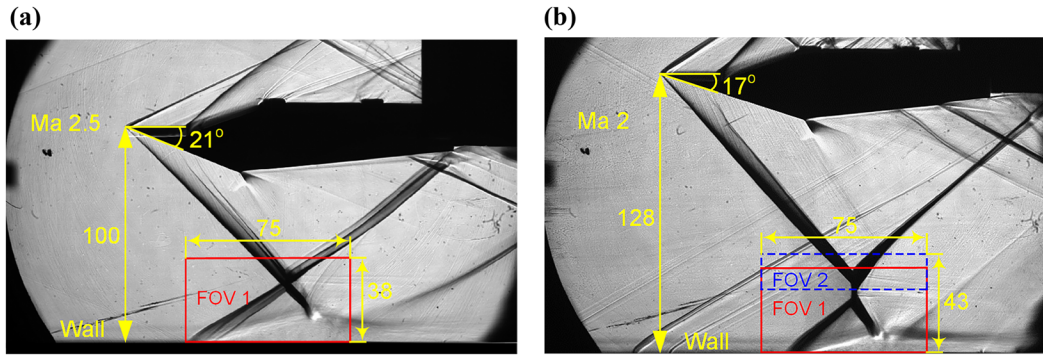
FIG. 4. FOVs in two experiments. (a) Mach 2.5, 21°. (b) Mach 2.0, 17°.

uniformization of the wind tunnel, and then, the diameter and density could only be estimated roughly because the accurate measurement by a microscope is unavailable online; (2) the liquid particle is greatly affected by the environmental temperature which decreases seriously in the supersonic flow, resulting in the particle condensation. Thus, in the supersonic PIV experiment, an oblique shock wave is generally used to quantitatively evaluate the particle relaxation.[41,47,48] The theoretical particle velocity across the shock wave is

$$u_n(t) = (u_{n1} - u_{n2}) \cdot e^{-\frac{t}{\tau_p}} + u_{n2}, \qquad (9)$$

where u_n represents the velocity component normal to shock wave, subscripts 1 and 2 denote front and back of shock wave, and e is natural constant. Define u^* as

$$\ln(u^*) = \ln\left(\frac{u_n(t) - u_{n2}}{u_{n1} - u_{n2}}\right) = -\frac{t}{\tau_p}. \qquad (10)$$

When the front Mach number normal to the shock wave does not exceed 2, an approximate relation between τ_p and ξ_p can be obtained as follows:[42]

$$\ln(u^*) = -\frac{t}{\tau_p} \approx -\frac{S}{\xi_p}, \qquad (11)$$

where S is the displacement component normal to the shock wave. The distribution of $u*$ with S in the shock-normal direction can be achieved based on the velocity field measured by PIV. Then, the particle relaxation distance is easily calculated by fitting the experimental

data according to Eq. (11), and finally, the more practical relaxation time is obtained by Eq. (8).

In this work, we use the stronger oblique shock wave generated by the 21° wedge model in the freestream of Mach 2.5 to evaluate the particle tracking performance. The shock-normal velocity component field is shown in Fig. 6(a). The experimental data of u^* with S along the shock-normal direction are fitted by the theoretical model of Eq. (11), with an average filter on account of the velocity averaging effect caused by interrogation window and interval time of dual-pulse laser. According to the result of Fig. 6(b), the particle relaxation time/distance is 2.0 μs/0.7 mm, which fully meets the measurement requirements of supersonic PIV experiments.[42]
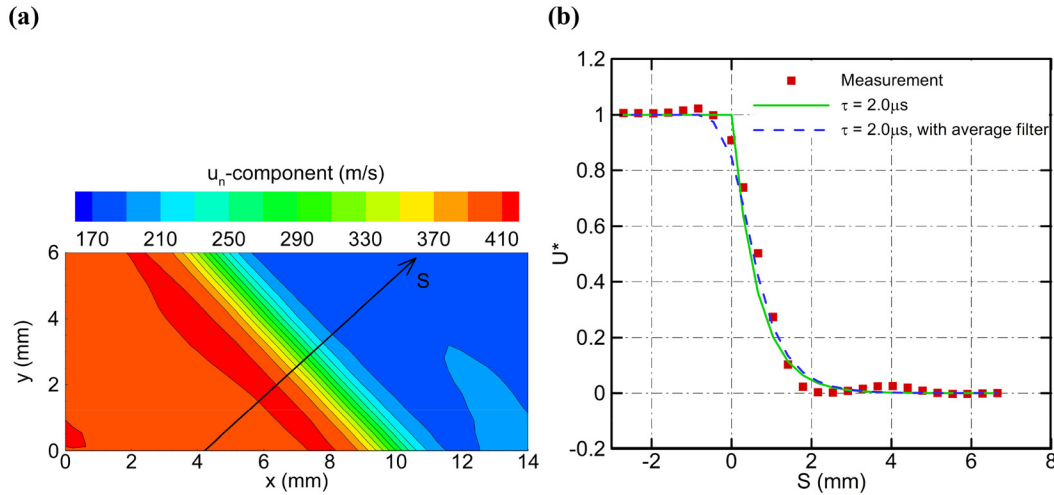
III. EVALUATION OF VELOCITY FIELD

The application of PIV in the strong SWBLIs is a great challenge, while the quality of velocity data directly affects the accuracy of pressure reconstruction. Therefore, this section would provide detailed evaluations for the boundary layers, time-averaged velocity fields, and turbulence properties of the two SWBLIs based on the PIV measurement data.

FIG. 5. Instantaneous particle image of SWBLI (Mach 2.0, Mach reflection).

TABLE II. PIV recording and post-processing parameters.

Parameter	EXP 1 and EXP 2
PIV recording	
Particle relaxation time (μs)	2.0
Laser frequency (Hz)	15
Pulse separation Δt (μs)	2.3
CCD resolution (pixel^2)	1623×1235
Lens aperture $f_\#$	5.6
Digital resolution (μm/pixel)	47.5
Field of view, $W \times H$ (mm^2)	75×38 (EXP 1); 75×43 (EXP 2)
Post-processing	
Initial interrogation window (pixel^2)	64×64
Final interrogation window (pixel^2)	32×32
Overlap ratio	75%
Number of iterations	5

(a)

(b)

FIG. 6. Evaluation of particle relaxation based on oblique shock wave generated by 21° wedge in Mach 2.5 freestream. (a) Shock-normal velocity component field. (2) Distribution of u^* with S in shock-normal direction.
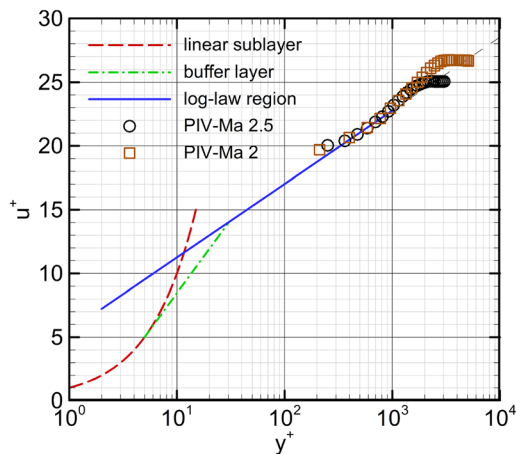
A. Boundary layer

The analyses for the boundary layers are mainly to evaluate the impact of laser reflection on PIV data and prove the feasibility of surface blackening scheme. The measurement accuracy of the boundary layers is assessed by a comparison with the theoretical results of typical characteristics. In addition, the boundary layer thickness is obtained to define the related dimensionless parameters.

In general, the time-averaged streamwise velocity component $\overline{u}$ and wall-normal distance y in the boundary layer are non-dimensionalized by the friction velocity u_τ,

$$u^+ = \frac{\overline{u}}{u_\tau}, \quad y^+ = \frac{u_\tau y}{\nu_w}, \quad u_\tau = \sqrt{\frac{\tau_w}{\rho_w}}, \quad (12)$$

where ν_w and τ_w denote the dynamic viscosity and the shear stress on the wall. Figure 7 shows the theoretical velocity distributions and the

FIG. 7. Theoretical velocity distributions and PIV measurement results in boundary layers.

PIV measurement results inside the inner part of the boundary layer, which could achieve good agreement under u_τ of 22.9 and 19.3 m/s for EXP 1 and 2. The corresponding skin friction coefficients cf are calculated to be 1.54×10^{-3} and 1.62×10^{-3}, which agree well with the theoretical values by the van Driest II formula.[49] Because of the laser reflection on the wall and the limited spatial resolution, this PIV setup could only obtain reliable velocity data outside the log-law region. The closest valid data are 0.85 and 0.43 mm to the wall, where the measurement accuracy is still relatively low. The 99% boundary layer thickness δ in front of the FOV reaches 5.55 and 5.32 mm, corresponding to the Reynolds number Re_δ of 8.9×10^4 and 1.25×10^5. According to the comparison between experimental data and theoretical values, it can be concluded that the PIV arrangement described in Sec. II could effectively capture the supersonic boundary layer and then the separation region downstream.

B. Features of time-averaged velocity field

The time-averaged flow topologies of the SWBLIs are shown in Fig. 8, where the origin of y axis is set on the lower wall of the wind tunnel. The black contours present the distribution of wall-normal velocity component, which could well reflect the expansion and compression/shock waves in the flow field. The streamlines clearly show the separation bubbles and the flow angles. Due to the relatively strong incident shock waves, the separation bubbles are very large with the heights of 1.8δ (Mach 2.5)/1.5δ (Mach 2.0) and the widths exceed 8δ in the mean flow fields. As a result, the separation shocks intersect with the incident shocks outside the boundary layers, forming regular and Mach reflections. The reattachment points and the reattached shock waves downstream of the separation regions are not captured because of the limited FOV. In the Mach 2.5 measurement, the expansion wave fan emitted from the inflection point of the wedge model appears in the FOV but do not affect the main flow structures of the regular reflection, as shown in Fig. 8(a). It should be noted that the dimensionless widths of the FOVs in Figs. 8(a) and 8(b) are slightly different owing to the different boundary layer thickness.
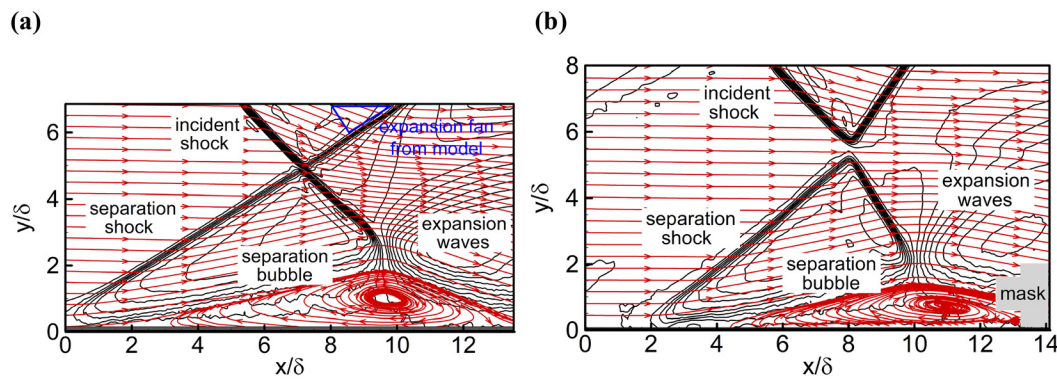
FIG. 8. Time-averaged flow topologies of SWBLIs. (a) Mach 2.5, 21°. (b) Mach 2.0, 17°.

As mentioned in Sec. II, the freestream Mach numbers are not exactly the same as the nominal values mainly due to the boundary layers. Therefore, a more accurate calibration is conducted based on the flow deflection angle of Fig. 8 and the shock angle of Fig. 9. According to Figs. 8(a) and 8(b), the streamlines upstream show the downward angles of about 0.65°/0.30°, which increase to about 21.26°/14.72° behind the incident shocks, resulting in the deflection angles θ of about 20.61°/14.42°. According to Figs. 9(a) and 9(b), the angles between the incident shocks and the lower tunnel walls are observed to be 45.51°/45.30°. Considering of the downward angles of 0.65°/0.30° upstream, the shock angles can be determined to be 44.86°/45.00°. Based on the calibrated deflection angles and shock angles, the actual Mach numbers upstream are obtained to be 2.42/1.98 by the oblique shock theory. It is noted that in the FOV of EXP 2, the flow deflection angle is only 14.72° which is much less than the wedge angle, and the angle between incident shock and lower wall is only 45.30°, which is much less than the initial 48.41°. This is mainly caused by the small step on the tunnel wall of the Mach 2.0 nozzle, as shown in Fig. 9(b), while the Mach 2.5 nozzle is very smooth.

Figure 10 shows the time-averaged velocity fields in terms of the streamwise component u. It can be observed that the significant optical distortions exist near the shock waves, caused by the refraction of particle scattered light emitting through the flow.[50] The gap between the model and the optical glass further exacerbates this phenomenon. Therefore, the anomalous velocity gradients appear near the shock

waves, especially behind the incident shock and before the Mach stem in Fig. 10(b). In addition, the strong SWBLIs present large fluctuations of the separation bubbles and the separation/reflected shock waves,[51] which may increase the measurement uncertainties of the mean velocity fields. According to the instantaneous velocity fields, the heights of separation regions fluctuate in the large ranges of $2.2\delta/1.4\delta$ and the separation points move within $2.8\delta/1.8\delta$. In addition, it is difficult to accurately measure the slip-lines downstream of the shock reflections, due to the limited spatial resolution of PIV. In a word, these adverse factors pose significant challenges for the applications of PIV-based pressure measurement in such complex supersonic flow fields.

C. Turbulence properties

The root-mean-squares of turbulent velocity components u' and v', denoted by $<u'>$ and $<v'>$, are displayed in Fig. 11. It is obvious that the turbulence concentrates near the separation bubble, shear layer, slip-line, and shock wave. The $<u'>$ and $<v'>$ keep the same order in the separation bubble and near the shock wave, implying the strong instability of the entire shock reflection. Compared with the stable incident shock waves, the separation/reflected shock waves show severe oscillations. In the Mach reflection, the Mach stem and the transmitted/reflected shocks with greater $<u'>$ indicate more intense streamwise fluctuations than the regular reflection. As the wedge angle increases from 17° to 21°, the turbulence intensity rises significantly in
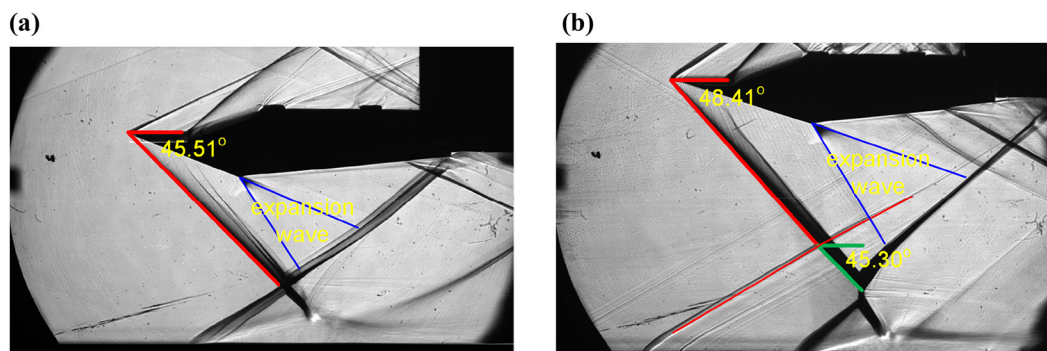

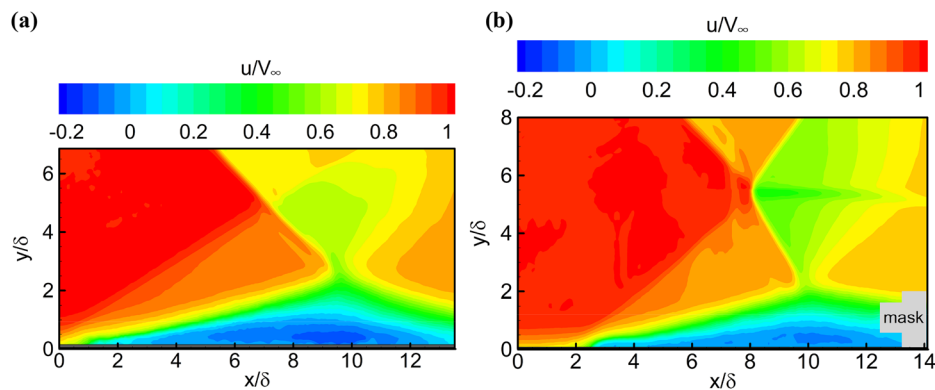**FIG. 9.** Instantaneous schlieren images of SWBLIs. (a) Mach 2.5, 21°. (b) Mach 2.0, 17°.

FIG. 10. Time-averaged velocity fields in terms of streamwise component u. (a) Mach 2.5, 21°. (b) Mach 2.0, 17°.

the boundary layer and the separation region, while the main flow remains at a low turbulence level.

Figure 12 further presents the distributions of various Reynolds stress terms for evaluating the influence of turbulent velocity on the reconstructed pressure field. First, in the mainstreams with the primary structures of regular/Mach reflections, the Reynolds stress is almost zero except for the shock "regions." However, in the supersonic flow with complex shock system, the essential problem of PIV-based pressure measurement is to accurately propagate the pressure information across the shock wave instead of obtaining the correct result "inside" the shock region,[33] because the accurate velocity measurement of the physical shock wave is impossible due to the particle relaxation. Thus, the influence of turbulence terms on the pressure reconstruction can be completely ignored in the mainstream. Second, $<u'v'>$ and $<v'v'>$ are one order of magnitude smaller than $<u'u'>$ in the shear layer

around the separation bubble, where the reconstructed pressure field can be integrated from the mainstream toward the wall in y direction to reduce the turbulence contribution, because the PIV measurement error for turbulent velocities generally exceed 10%.[33,48] In conclusion, the effect of the Reynolds stress terms should be carefully evaluated and then can be greatly reduced by adopting an appropriate reconstruction scheme to improve the accuracy of the pressure field.

IV. RECONSTRUCTION OF PRESSURE FIELD

Based on the detailed evaluation of the PIV velocity field, this section will comprehensively use the MacCormack, SLB, and CSI methods to conduct the pressure field reconstructions for the two strong SWBLIs. The feasibility and high accuracy of the proposed reconstruction scheme for complex supersonic flows will be fully verified compared with the theoretical results by the oblique shock relation, the free
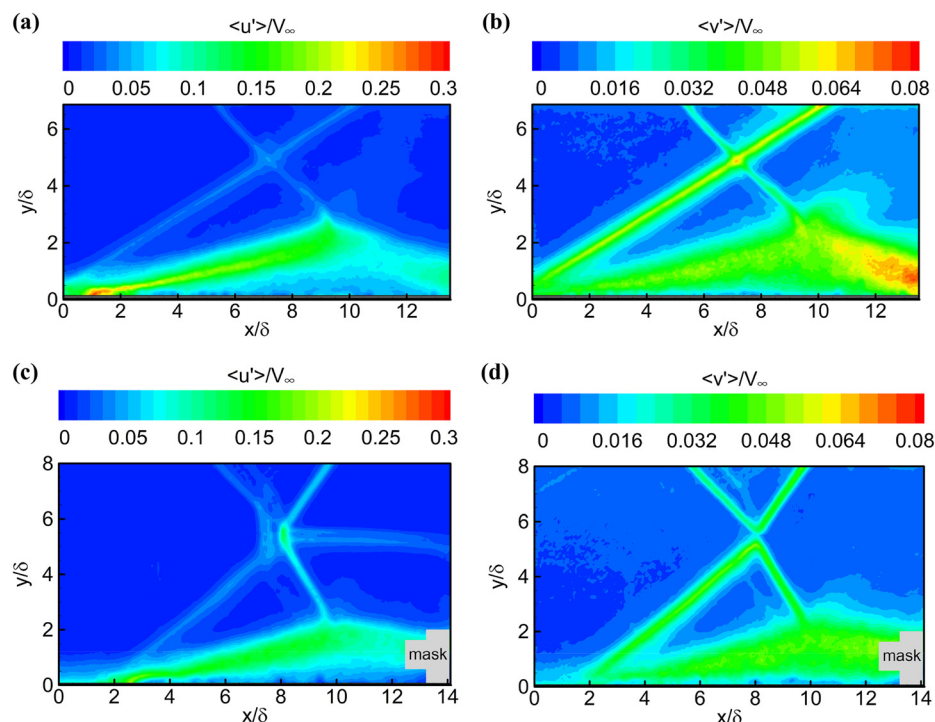

FIG. 11. Root-mean-squares of turbulent velocity components u' and v', denoted by $<u'>$, $<v'>$. (a) and (b) Mach 2.5, 21°. (c) and (d) Mach 2.0, 17°.
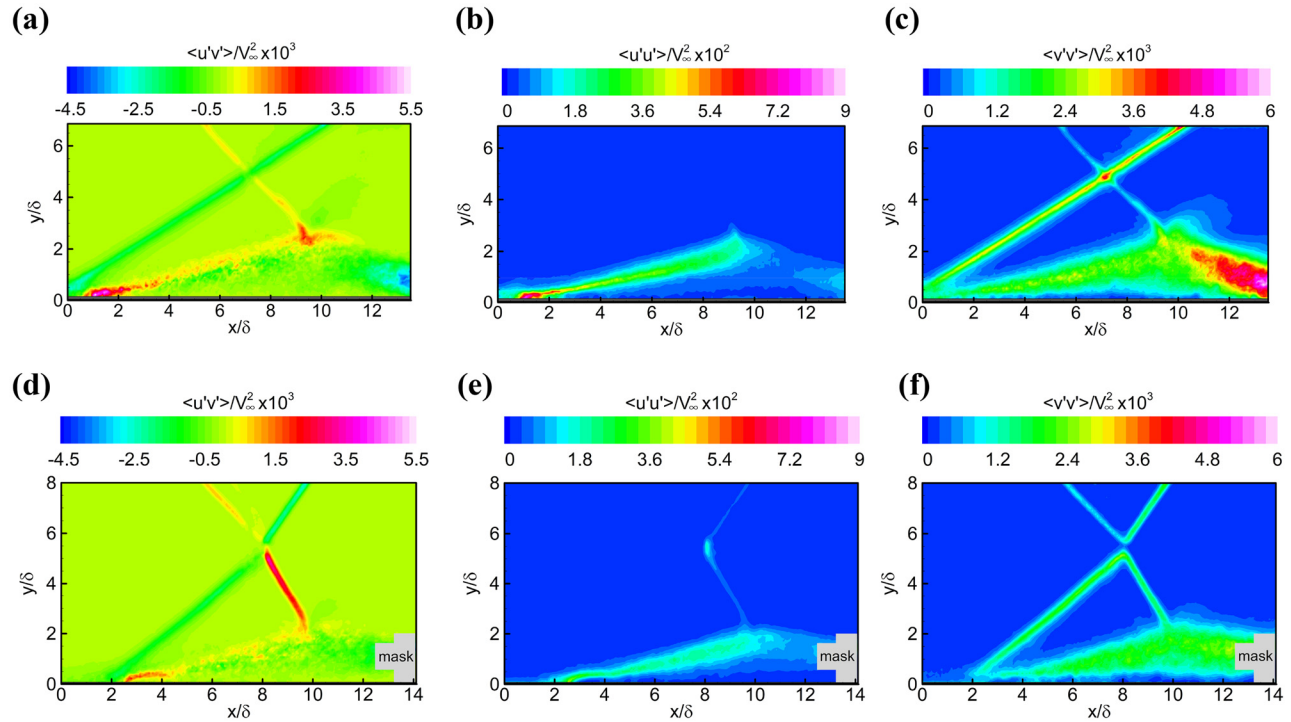
FIG. 12. Distributions of various Reynolds stress terms $<u'v'>$, $<u'u'>$ and $<v'v'>$. (a)–Mach 2.5, 21°. (d)–(f) Mach 2.0, 17°.

interaction theory, and the shock polar analysis, which finally confirms the applicability of PIV-based pressure measurement in academic research types and engineering tests of supersonic flows.

A. Scheme of pressure reconstruction

As mentioned in the introduction, although the MacCormack and the SLB methods had been experimentally validated by single oblique and bow shock waves, applying them to the supersonic flows with complex shock waves remains highly challenging, on account of the reconstruction error propagation across the shock wave and the reduced PIV measurement accuracy caused by the laser reflection, optical distortion, and severe flow unsteadiness. In addition, the SWBLI contains variable typical flow structures from the low-speed separation bubble and shear layer to the high-speed shock reflection, posing a greater challenge to the reliable pressure reconstruction. In

this condition, the most critical problem is to elaborately couple multi-algorithms to achieve an optimal reconstruction scheme for alleviating the pressure error accumulation as much as possible.

The reconstruction schemes are similar for the two SWBLIs, which need to be divided into four sub-regions according to the flow structures shown in Fig. 13. The most suitable reconstruction methods are evaluated and then adopted in different sub-regions to maximize their advantages, thereby obtaining a more accurate reconstructed pressure field.

1. MacCormack region

The MacCormack method overcomes the serious deterioration of the reconstructed pressure field across the strong shock wave,[35,36] and then, it is particularly suitable for the shock reflections in the mainstreams marked by the black rectangles in Fig. 13. The principle of this
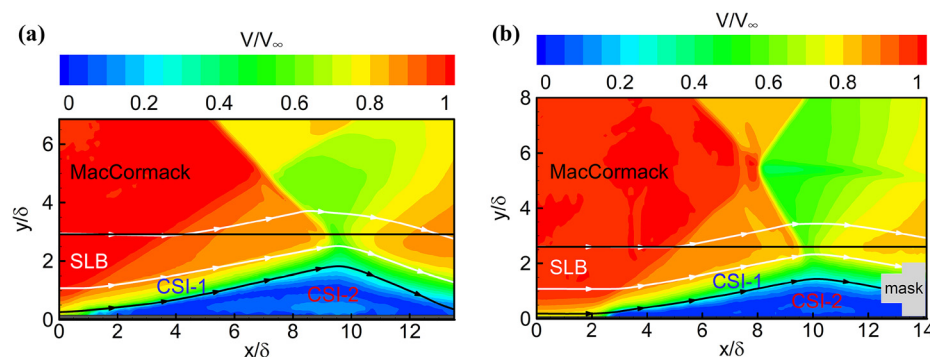

FIG. 13. Reconstruction schemes for SWBLIs. (a) Mach 2.5, 21°. (b) Mach 2.0, 17°.

method draws on MacCormack's technique in computational fluid dynamics, but the velocity components u and v have been measured by PIV, resulting in four unknown variables (density ρ, pressure p, temperature T, and internal energy e) in the N–S equations. Thus, four equations should be selected, including two equations of state (for closing the equation set), the combined momentum equation and the energy equation. Considering of the negligible effect of viscous terms on pressure reconstruction,[8] the basic equations of the MacCormack method are obtained as follows:

$$p = \rho R T; \; e = c_v T, \tag{13}$$

$$\frac{\partial U}{\partial t} = -\frac{\partial F}{\partial x} - \frac{\partial G}{\partial y}, \tag{14}$$

where c_v is the specific heat at constant volume, and

$$U = \begin{bmatrix} \rho(u+v) \\ \rho E \end{bmatrix}, \; F = \begin{bmatrix} \rho(u^2 + uv) + p \\ u(\rho E + p) + q_x \end{bmatrix}, \; G = \begin{bmatrix} \rho(uv+v^2) + p \\ v(\rho E + p) + q_y \end{bmatrix},$$

$$E = e + \frac{u^2 + v^2}{2}, \; q_x = -K\frac{\partial T}{\partial x}, \; q_y = -K\frac{\partial T}{\partial y},$$

where K is the thermal conductivity.

For time-averaged turbulent flows, the density fluctuation is generally neglected at medium Mach numbers.[32,33] Then, the momentum equation in Eq. (14) is simplified as

$$\frac{\partial[\overline{\rho}(\overline{u}+\overline{v})]}{\partial t} = -\frac{\partial\left[\overline{\rho}\left(\overline{u}^2 + \overline{u}\,\overline{v} + \overline{u'^2} + \overline{u'v'}\right) + \overline{p}\right]}{\partial x}$$
$$-\frac{\partial\left[\overline{\rho}\left(\overline{u}\,\overline{v} + \overline{v}^2 + \overline{u'v'} + \overline{v'^2}\right) + \overline{p}\right]}{\partial y}. \tag{15}$$

In addition, the energy equation in Eq. (14) could be replaced by the simple algebraic Eq. (16) under the adiabatic assumption, which is valid in most of the wind tunnel experiments without severe heat transfer,[24,25] to reduce the numerical error during the time-marching iterative solution

$$\frac{\overline{T}}{T_\infty} = 1 + \frac{\gamma-1}{2}M_\infty^2\left(1 - \frac{\overline{V}^2 + \overline{V'^2}}{V_\infty^2}\right). \tag{16}$$

Although the MacCormack method shows great advantages in strong shock flows, it requires more elaborate boundary condition. The velocity measurement error of PIV is relatively large in the separation region with severe oscillation, and then, the lower boundary of the MacCormack region is located outside the shear layer, as shown in Fig. 13. The left boundary is in the freestream where the Dirichlet condition can be obtained based on Eq. (3). The other three boundaries are given by the Neumann conditions based on Eq. (6). For the mean turbulent flow, Eq. (6) should be written in the time-averaged form

$$\left(\delta_{ij} + \frac{\overline{u_i u_j} + \overline{u'_i u'_j}}{R\overline{T}}\right)\frac{\partial\ln\left(\overline{p}/p_\infty\right)}{\partial x_j}$$
$$= -\frac{1}{R\overline{T}}\left(\frac{\partial\left(\overline{u_i u_j} + \overline{u'_i u'_j}\right)}{\partial x_j} - \frac{\overline{u_i u_j} + \overline{u'_i u'_j}}{\overline{T}}\frac{\partial\overline{T}}{\partial x_j}\right). \tag{17}$$

Finally, the time-marching iterative solution is performed based on MacCormack' technique

$$U_{i,j}^{t+\Delta t} = U_{i,j}^t + \left(\frac{\partial U}{\partial t}\right)_{av} \cdot \Delta t, \tag{18}$$

where $(\partial U/\partial t)_{av}$ represents the average value of $\partial U/\partial t$ in the time interval Δt, which is obtained by a predictor–corrector scheme. The detailed implementations could refer to Ref. 35.

2. SLB region

Considering of the poor spatial flexibility of the MacCormack method, it is more applicable to a regular FOV. In contrast, the more flexible SI method cannot obtain correct pressure field behind the strong shock wave. Thus, the SLB method is skillfully adopted between the MacCormack region and the shear layer, divided by the two white streamlines shown in Fig. 13. The principle of the SLB method is mainly based on the continuity equation in integral form, which shows better numerical stability across the shock wave.[38] For the one-dimensional tube flow, the basic equation could be simplified as

$$\rho_1 u_1 A_1 = \rho_2 u_2 A_2, \tag{19}$$

where A is the cross-sectional area of the flow tube, and subscripts 1 and 2 represent the positions of inlet and downstream. Based on the velocity field, a set of streamlines are traced from the left boundary, forming several one-dimensional flow tubes. Then, the density distributions along the flow tubes could be obtained as follows:

$$\rho_2 = \frac{\rho_1 u_1 A_1}{u_2 A_2}, \tag{20}$$

where the variables on the right side are known or measured by PIV. Finally, the pressure field is achieved by combining the adiabatic assumption of Eq. (4) and the ideal gas equation of state. The detailed implementations could refer to Ref. 38.

As for the two SWBLIs in this paper, the upper boundaries of the SLB regions are determined by the streamlines traced from the left boundaries at $y/\delta = 2.89$ (21°) and 2.58 (17°), while the lower boundaries are traced from the same dimensionless point of $y/\delta = 1.08$. The SLB region is entirely located exactly outside the shear layer where the velocity error is relatively small, thus ensuring the reconstruction accuracy of the pressure field. A total of 18 streamlines (including the upper and lower boundaries) are traced from the upstream with an equal initial spacing of about 0.59 mm. Considering of the turbulence effect, the final position of each streamline is taken as the average of the streamlines based on instantaneous velocity fields. As a result, the mean vertical height of the 17 flow tubes behind the separation shock is about 0.38 mm, which is consistent with the velocity vector resolution, for achieving an accurate interpolation of the local velocity and sectional area along the flow tube. In addition, the spacing between adjacent nodes in the streamwise direction is also set to 0.38 mm for the same purpose. The reconstructed pressure field in the overlapping part of the SLB and MacCormack regions is determined by the average result of the two methods.

3. CSI-1 region

It is difficult to achieve sufficient measurement accuracy in the shear layer due to the limited spatial resolution of PIV, especially for the streamwise velocity component u with large gradient in transverse direction. This would lead to a poorer accuracy of streamline tracking

and then reduce the reliability of the SLB method. Therefore, the more flexible CSI method based on Eq. (17) is adopted in the shear layer around the separation bubble, namely, CSI-1 region in Fig. 13. For the two SWBLIs, the CSI-1 regions are composed of the lower boundaries of the SLB regions and the streamlines traced from $y/\delta = 0.25$ (21°)/ 0.2 (17°) upstream. In addition, the effect of turbulence terms with relatively large measurement error would be minimized by a proper integration scheme.

As mentioned in Sec. III B, $<u'v'>$ and $<v'v'>$ are much smaller than $<u'u'>$ in the shear layer. Therefore, the spatial integration would be conducted from the pressure boundary in the main flow toward the wall in y direction, which could prevent using the data of u with large error and reduce the effect of turbulence terms. Figure 14 shows the grid meshing and the implementation of the CSI method. Each row/column is evenly divided into 199/14 nodes, with the horizontal/vertical spacing equivalent to the PIV data resolution. The boundary condition is prescribed with the reconstructed pressure on the lower streamline of the SLB region, and then, the spatial integration is performed row by row downward. Each unknown point is determined by the average of 2 or 3 integration results along different paths, which is similar to the traditional multi-path SI method.

4. CSI-2 region

The remaining CSI-2 region (mainly including the separation bubble) is surrounded by the lower boundary of CSI-1 region and the wall, as shown in Fig. 13. It is an irregular subsonic flow region, where the flexible CSI method is also more suitable. The integration mesh is completely consistent with the PIV data, and the boundary condition is given by the reconstructed pressure on the lower streamline of CSI-1 region, as shown in Fig. 15. Then, the spatial integration is performed column by column downstream. Each unknown point is determined by the average of 2–4 integration results along different paths.

Finally, a multiple median filter with kernel sizes of 7×7, 5×5, and 3×3 is applied to the initial reconstructed pressure fields composed of the sub regions by different methods, to further improve the reconstruction accuracy and eliminate the slight discontinuities near the boundaries of adjacent sub regions. It is noted that the filter is abandoned near the shock waves to prevent the serious error diffusion.

B. Evaluation of reconstructed pressure fields

Figure 16 shows the final reconstructed pressure fields of the two SWBLIs. A qualitative evaluation would be conducted at first. It can be observed that although each pressure field is composed of four sub regions by different methods, no obvious discontinuity appears in the pressure contour. The pressure is uniformly distributed behind the incident shock, while it remains almost constant within the entire separation region with the wall-normal pressure gradient of about zero. The compression waves converging into the separation shock are clearly visible in the boundary layer. The incident shock penetrates through the separation shock and then reflects at the shear layer to form an expansion wave fan, where the reconstructed pressure contour shows the equivalent pattern to the velocity field. Although the limited spatial resolution of PIV makes it difficult to accurately measure the slip-line downstream of the shock reflection, there is almost no visible impact on the reconstructed pressure field, especially near the Mach reflection in Fig. 16(b). These results are in good agreement with the
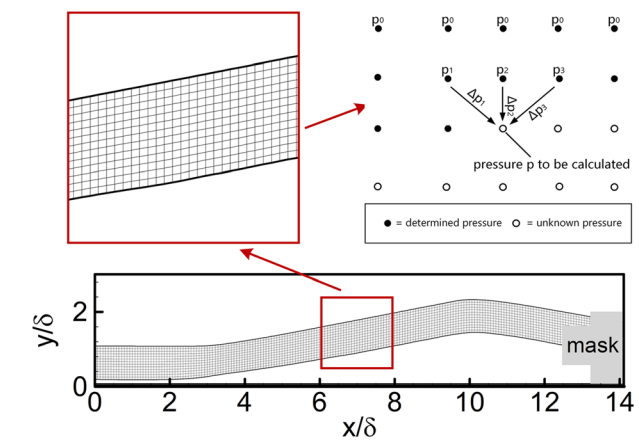

FIG. 14. Grid meshing and implementation of CSI method in CSI-1 region (Mach 2.0, 17°).

physical phenomena, thus preliminarily proving the feasibility of the coupling pressure reconstruction scheme.

The quantitative accuracy of the pressure reconstruction will be assessed with the theoretical solutions in typical regions of the SWBLIs. First, the pressure distributions behind the incident shocks (along S direction in Fig. 16) are compared with the results by the oblique shock relation, as shown in Fig. 17. According to the discussion in Sec. III B, these two incident shocks are actually generated by the wedge angles of 20.61°/14.42° in the freestream of Mach 2.42/1.98, corresponding to theoretical pressure ratios of 3.233/2.124. Due to the close proximity of the S-axis to the incident shock, the velocity measurement error is relatively large nearby. In addition, the median filter applied to the initial reconstructed pressure field avoids the region near the shock wave to prevent the error diffusion, as described in Sec. IV A. Thus, the reconstructed pressure distributions along the S-axis exhibit slight oscillations around the reference theoretical values but no significant biased errors, as shown in Fig. 17, where the negative
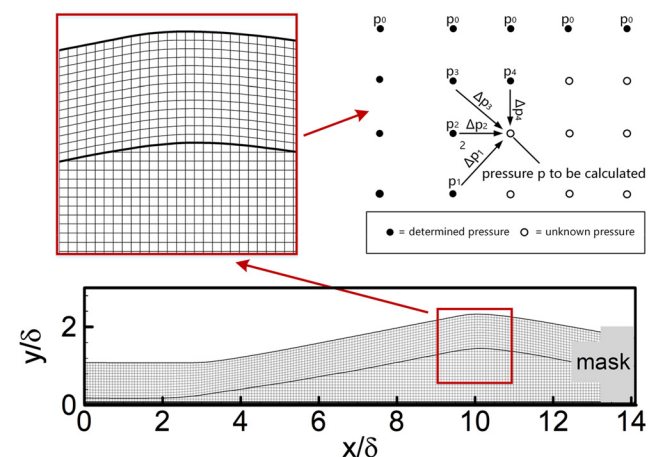

FIG. 15. Grid meshing and implementation of CSI method in CSI-2 region (Mach 2.0, 17°).
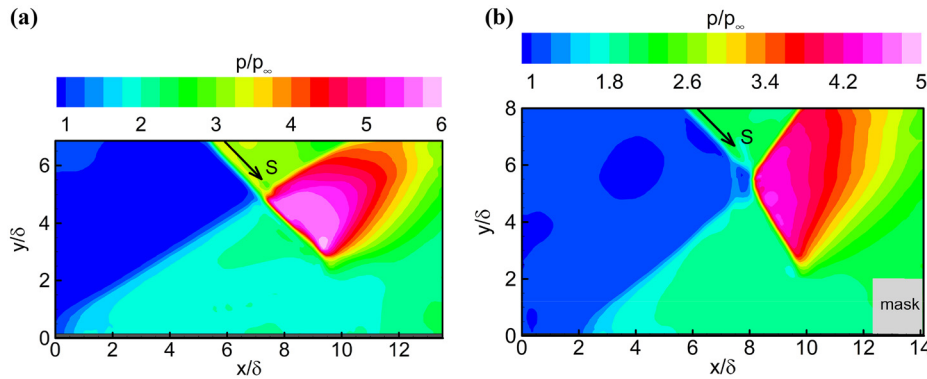
FIG. 16. Reconstructed pressure fields of SWBLIs. (a) Mach 2.5, 21°. (b) Mach 2.0, 17°.

relative error is converted to the positive value. The average reconstructed pressure ratios are 3.232/2.120, with the relative errors of only 0.03%/0.19% and the maximum local errors within 2.5%/1.7%.

Then, the free interaction theory of Eq. (21) is adopted to evaluate the pressure reconstruction across the separation shock near the wall

$$\frac{p}{p_\infty} = 1 + F(\overline{x})\frac{\gamma}{2}M_\infty^2\sqrt{\frac{2c_f}{(M_\infty^2 - 1)^{1/2}}}, \quad (21)$$

where the skin friction coefficient c_f has been obtained in Sec. III A, and $F(\overline{x})$ represents a general correlation function. In the SWBLI, the values of $F(\overline{x})$ are about 4.22 near the separation point and 6 for the pressure plateau,[52] corresponding to pressure ratios of 1.65/1.92 (Mach 2.5) and 1.50/1.72 (Mach 2.0). Considering that PIV is unable to obtain valid data on the wall and the measurement accuracy is relatively low in the initial valid data closest to the wall (see Fig. 7), the reconstructed pressure in the second row is approximated as the wall pressure here, and its distribution across the separation shock wave is plotted in Fig. 18. To reduce the effect of PIV random error on the pressure reconstruction, a cubic curve is used to fit the reconstructed pressure distribution. The circular and diamond symbols on the fitted curve denote the theoretical pressure ratios of the separation point and

the pressure plateau, respectively. The separation of the boundary layer leads to the separation shock wave which manifests as a series of compression waves within the boundary layer, causing a rapid pressure increase. Within the separation bubble, the wall pressure is maintained at a plateau. The reattachment shock wave downstream would make the wall pressure rise again, but this part of the flow field is not captured due to the limited FOV. Compared with the mean u-velocity field of Fig. 10, it can be seen that the separation points measured by PIV are located about 1.6δ and 1.5δ backward. These results based on the time-averaged velocity fields are already better than expected, considering of the large-amplitude and high-frequency oscillations of the separation bubbles and the large velocity measurement error near the wall. As for the pressure plateau, the relative errors between the reconstructed results (1.98/1.80) and the theoretical values (1.92/1.72) are about 3.1% and 4.7%, which are basically acceptable in academic research types and engineering measurements.

For the regular reflection induced by the 21° wedge, the separation shock angle is calculated to be about 34.09° based on the reconstructed pressure ratio at the plateau, which agrees well with the angles of 33.74° in the flow topology of Fig. 8(a) and 33.55° by the free interaction theory. For the Mach reflection induced by the 17° wedge, the separation shock angle is about 40.96° according to the reconstructed
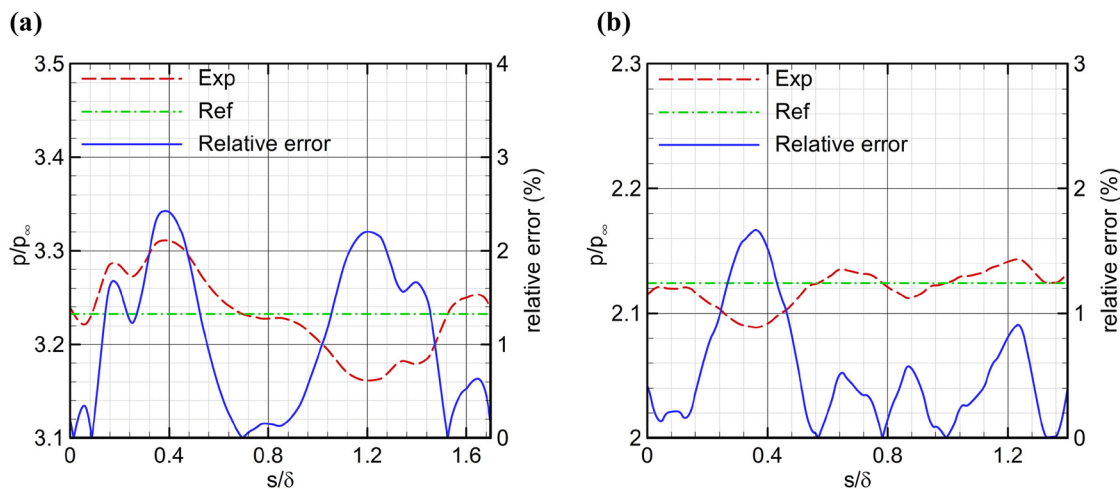

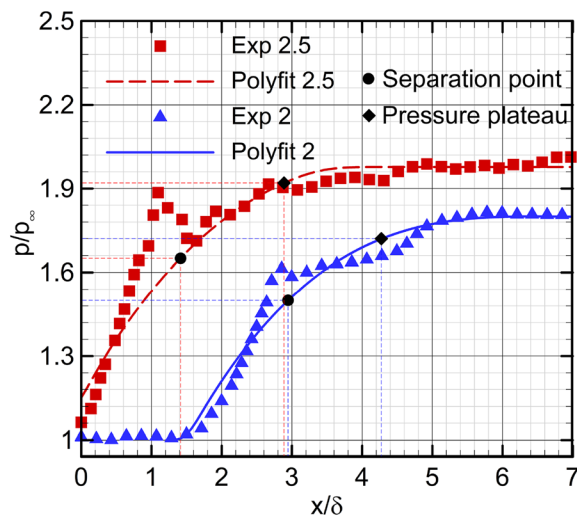**FIG. 17.** Reconstructed pressure distributions along S-axis. (a) Mach 2.5, 21°. (b) Mach 2.0, 17°.

FIG. 18. Pressure distributions across separation shock waves.

pressure plateau. This result is also close to the angles of 41.54° in Fig. 8(b) and 39.97° by the theory, but the agreements are not as good as the regular reflection because the Mach reflection is more unsteady as described in Sec. III C. These results further verify the high accuracy of the reconstructed pressure fields from another perspective.

Finally, according to the flow deflection angle and shock angle at the shock reflection point, the reconstruction accuracy downstream will be analyzed through the theoretical shock polar. For the regular reflection, it can be observed from Fig. 8(a) that the deflection angles across the separation/incident shocks are 10.99°/20.61° near the reflection point, and then the corresponding shock polar can be plotted in Fig. 19(a). Based on this result, the theoretical pressure ratio can be obtained as about 5.67 downstream of the reflection point, where the locally averaged reconstructed pressure ratio in Fig. 16(a) is about 5.58 with a relative error of about 1.59%. As for the Mach reflection, the

topology of Fig. 8(b) shows the flow deflection angle across the separation shock of about 11.60° near the lower triple point of the shock reflection, and the incident shock causes a deflection angle of about 14.42°. Then, the corresponding shock polar is plotted in Fig. 19(b). It can be obtained that the theoretical pressure ratios downstream of the upper and lower triple points are about 4.40 and 4.41, respectively. In contrast, the reconstructed pressure ratios in Fig. 16(b) are about 4.30 and 4.48 with the acceptable relative errors of 2.27% and 1.59%.

In summary, this section provides quantitative analyses for the pressure reconstruction based on three typical flow regions with theoretical solutions, including the incident shock, the separation shock, and the shock reflection. These detailed evaluations comprehensively verify the high accuracy of the entire reconstructed pressure field. Under the various uncertain factors in the PIV experiment, such as the model manufacturing and installation, the surface planeness of the wind tunnel, and the random error in PIV measurement, the accuracy and stability achieved by the proposed pressure reconstruction scheme could fully meet the measurement requirements in fundamental research types and engineering applications.

C. Effect of Reynolds stress terms

In PIV-based pressure measurements, the Reynolds stress terms generally should be taken into account,[32] but their measurement accuracy is usually poor as explained in Sec. III C. Therefore, the pressure reconstruction scheme in Sec. IV A aims to avoid the negative impact of the large turbulent velocity measurement error on the reconstructed pressure field as much as possible, by adopting an appropriate integration path. In this section, the contribution of turbulence terms in the proposed reconstruction scheme will be evaluated quantitatively for the two strong SWBLIs.

The "laminar" pressure reconstruction strictly follows the scheme and principle in Sec. IV A only with turbulence terms neglected. The reconstructed pressure fields are shown in Fig. 20, which has almost no visible difference compared with the "turbulent" results in Fig. 16. Therefore, Fig. 21 further provides the quantitative discrepancy between the two results. Obviously, the turbulence contribution is
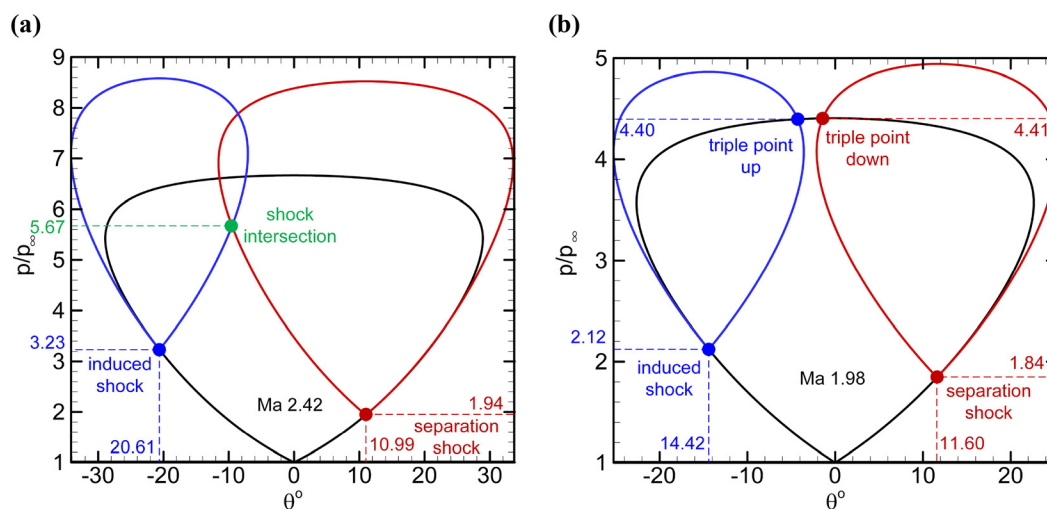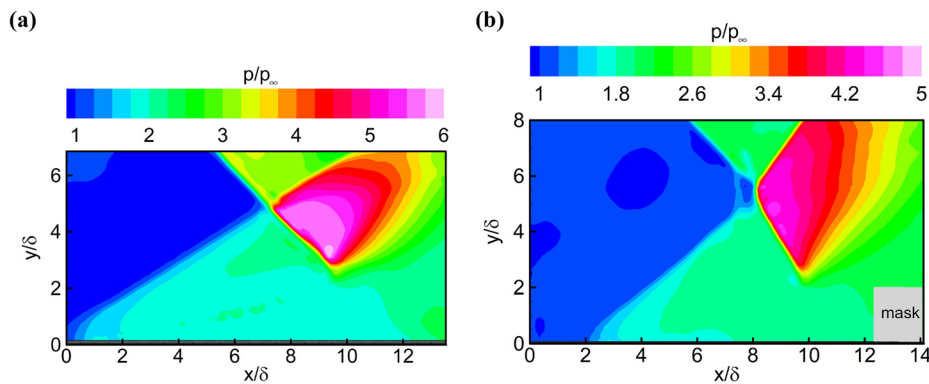

FIG. 19. Shock polar analyses for reflection points. (a) Mach 2.5, 21°. (b) Mach 2.0, 17°.

FIG. 20. Reconstructed pressure fields of SWBLIs (without turbulence terms). (a) Mach 2.5, 21°. (b) Mach 2.0, 17°.

almost zero in the freestream and downstream of the incident/separation shock waves, while a slight increase appears in the expansion region behind the shock reflection. However, overall, in the mainstream, the contribution outside the shock "region" is mostly less than 0.01 and will further decrease with the weakening of the incident shock. It should be emphasized once again that the most critical problem in PIV-based pressure measurement for shock flows is to correctly propagate the pressure information across the strong shock wave, instead of focusing on the shock region caused by particle relaxation where the larger turbulence contribution has no practical significance. For the shear layer around the separation bubble, the influence of turbulence terms decreases obviously as the incident shock weakens. However, even in the stronger SWBLI induced by 21° wedge, the maximum contribution is less than 0.03. The size and turbulence intensity of the separation region increase greatly with the enhancement of incident shock. However, the turbulence contribution is still limited to 0.04 in the majority of the separation bubble induced by 21° wedge, while it further reduces to less than 0.03 in the other case. It is worth noting that the turbulence contributions mentioned above are all non-dimensionalized by the freestream pressure. In fact, if the non-dimensionalization takes the truth value of local pressure as the reference, the dimensionless turbulence contribution would be much smaller.

In conclusion, although the flow oscillations in the strong SWBLIs show high frequency and large amplitude, the effect of turbulence terms concentrates on the wall near the separation region, but it is mostly limited within 2% (based on local theoretical pressure) in the boundary layer. As for the main flow, the turbulence effect can be

completely neglected. Furthermore, considering of the large measurement error of turbulent velocities, the turbulence terms in the basic equations are reasonable to be omitted by using the proposed pressure reconstruction scheme in most academic research types and engineering tests.

V. CONCLUSIONS

This paper proposes a coupling scheme of PIV-based pressure measurement especially for the complex supersonic flows with strong shock waves, by adopting the MacCormack, SLB, and CSI methods. Based on the proposed reconstruction scheme, the pressure fields are well obtained for the two strong SWBLIs with the regular and Mach reflections, which are induced by the oblique shock waves generated by the wedge models of 21° and 17° in the freestream of Mach 2.5 and 2.0. Compared with the oblique shock relation, free interaction theory, and shock polar analysis, the reconstruction results confirm the feasibility and high accuracy of the proposed scheme and may promote its application to academic research types and engineering tests in strong shock flows.

The detailed evaluations for the typical flow structures are the great foundation for proposing the proper reconstruction scheme. This PIV setup could obtain reliable velocity data outside the log-law region of the boundary layer. The closest valid data are 0.85 and 0.43 mm to the wall for the two SWBLIs. PIV measurement results agree well with the theory under u_τ of 22.9/19.3 m/s and cf of 1.54/1.62×10^{-3}. The boundary layer thickness is 5.55/5.32 mm corresponding to Re_δ of $0.89/1.25 \times 10^5$. According to the velocity fields and schlieren images, the deflection angles and shock angles are
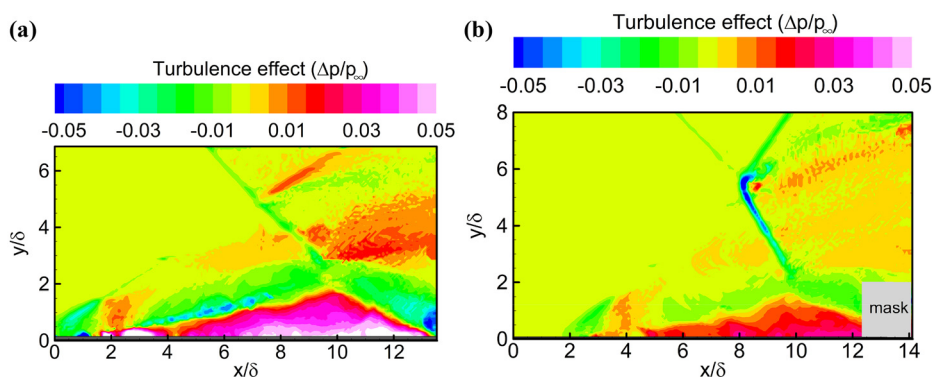
FIG. 21. Contribution of turbulence terms to reconstructed pressure fields. (a) Mach 2.5, 21°. (b) Mach 2.0, 17°.

calibrated to be 20.61°/14.42° and 44.86°/45.00°, achieving the real freestream Mach numbers of 2.42/1.98. The influence of turbulence terms on the pressure reconstruction can be ignored in the mainstream. In the shear layer, the spatial integration can be conducted from the mainstream toward the wall in y direction to reduce the turbulence contribution.

The MacCormack method is particularly suitable for the shock reflection in the mainstream, while the SLB method is adopted between the MacCormack region and the shear layer. Due to the insufficient measurement accuracy in the shear layer, the more flexible CSI method is used with a proper integration path for reducing the turbulence contribution. As for the irregular separation region, the flexible CSI method is also more applicable than the other methods. Based on this scheme, the pressure fields are well reconstructed. The pressure ratios behind the incident shock waves are 3.232/2.120 with the relative errors of 0.03%/0.09%, compared with the theoretical results of 3.233/2.22 by the oblique shock relation. According to the free interaction theory, the separation points measured by PIV are located about 1.6δ and 1.5δ backward, and the relative errors at the pressure plateau are about 3.1% and 4.7%. As for the shock reflections, the shock polar analyses are used for the evaluations. The reconstructed pressure ratio is about 5.58 with a relative error of 1.59% downstream of the regular reflection point. In the Mach reflection, the pressure ratios are about 4.30 and 4.48 with the relative errors of 2.27% and 1.59% downstream of the upper and lower triple points. The effect of turbulence terms concentrates on the wall near the separation region but is mostly limited within 2% in the boundary layer.

In conclusion, the accuracy and stability of the proposed pressure reconstruction scheme for supersonic flows with intense shock systems could fully meet the measurement requirements in fundamental research types and engineering applications.

AUTHOR DECLARATIONS
Conflict of Interest

The authors have no conflicts to disclose.

Author Contributions

Shun Liu: Conceptualization (lead); Data curation (lead); Formal analysis (lead); Funding acquisition (lead); Investigation (lead); Methodology (lead); Project administration (lead); Validation (lead); Visualization (lead); Writing – original draft (lead). **Jing Chen:** Validation (equal); Writing – review & editing (equal). **Bas W. van Oudheusden:** Resources (lead); Supervision (lead). **Jinglei Xu:** Supervision (equal); Writing – review & editing (equal). **Ferry Schrijer:** Resources (equal); Supervision (equal). **Bo Gao:** Funding acquisition (equal).

DATA AVAILABILITY

The data that support the findings of this study are available from the corresponding authors upon reasonable request.

REFERENCES

[1] M. Raffel, C. E. Willert, F. Scarano *et al.*, *Particle Image Velocimetry: A Practical Guide* (Springer, 2018).

[2] K. Wang, C. Kong, L. Wang *et al.*, "Flowfield reconstruction in a supersonic isolator based on proper orthogonal decomposition and sensor compression coupling under variable Mach numbers," Phys. Fluids **36**(10), 106130 (2024).

[3] D. Wang, Z. Wang, J. Chang *et al.*, "Experimental study on dynamic characteristics of shock train in an isolator with different types of incident shocks," Phys. Fluids **36**(7), 076108 (2024).

[4] C. Zhang, H. Zhang, G. Huang *et al.*, "Investigating the mechanism of flow of transonic compact crossover tandem diffuser," Phys. Fluids **36**(7), 077157 (2024).

[5] X. Chen, Z. Feng, and Q. Ye, "Amplitude modulation in turbulent boundary layer over anisotropic porous wall," Phys. Fluids **36**(2), 025127 (2024).

[6] A. D'Aguanno, F. F. J. Schrijer, and B. W. van Oudheusden, "Spanwise organization of upstream traveling waves in transonic buffet," Phys. Fluids **33**(10), 106105 (2021).

[7] J. Xiang, H. Zong, Y. Wu *et al.*, "Experimental control of the flow separation behind a backward facing step using deep reinforcement learning," Phys. Fluids **36**(10), 105102 (2024).

[8] B. W. Van Oudheusden, "PIV-based pressure measurement," Meas. Sci. Technol. **24**(3), 032001 (2013).

[9] T. Baur, "PIV with high temporal resolution for the determination of local pressure reductions from coherent turbulence phenomena," in *Proceedings of the 3rd International Workshop on PIV-Santa Barbara* (Springer, Heidelberg, 1999), pp. 101–106.

[10] R. Gurka, A. Liberzon, D. Hefetz *et al.*, "Computation of pressure distribution using PIV velocity data," in Workshop on Particle Image Velocimetry, 1999, Vol. 2.

[11] D. Violato, P. Moore, and F. Scarano, "Lagrangian and Eulerian pressure field evaluation of rod-airfoil flow from time-resolved tomographic PIV," Exp. Fluids **50**, 1057–1070 (2011).

[12] D. Ragni, B. W. Van Oudheusden, and F. Scarano, "Drag coefficient accuracy improvement by means of particle image velocimetry for a transonic NACA0012 airfoil," Meas. Sci. Technol. **22**(1), 017003 (2011).

[13] N. Fujisawa, S. Tanahashi, and K. Srinivas, "Evaluation of pressure field and fluid forces on a circular cylinder with and without rotational oscillation using velocity data from PIV measurement," Meas. Sci. Technol. **16**(4), 989 (2005).

[14] F. Auteri, M. Carini, D. Zagaglia *et al.*, "A novel approach for reconstructing pressure from PIV velocity measurements," Exp. Fluids **56**, 45 (2015).

[15] C. He and Y. Liu, "Time-resolved reconstruction of turbulent flows using linear stochastic estimation and sequential data assimilation," Phys. Fluids **32**(7), 075106 (2020).

[16] D. Fan, Y. Xu, H. Wang *et al.*, "Comparative assessment for pressure field reconstruction based on physics-informed neural network," Phys. Fluids **35**(7), 077116 (2023).

[17] X. Liu and J. Katz, "Instantaneous pressure and material acceleration measurements using a four-exposure PIV system," Exp. Fluids **41**(2), 227–240 (2006).

[18] J. J. Charonko, C. V. King, B. L. Smith *et al.*, "Assessment of pressure field calculations from particle image velocimetry measurements," Meas. Sci. Technol. **21**(10), 105401 (2010).

[19] Z. Wang, Q. Gao, C. Wang *et al.*, "An irrotation correction on pressure gradient and orthogonal-path integration for PIV-based pressure reconstruction," Exp. Fluids **57**, 104 (2016).

[20] B. W. Van Oudheusden, F. Scarano, and E. W. F. Casimiri, "Non-intrusive load characterization of an airfoil using PIV," Exp. Fluids **40**, 988–992 (2006).

[21] Y. Murai, T. Nakada, T. Suzuki *et al.*, "Particle tracking velocimetry applied to estimate the pressure field around a Savonius turbine," Meas. Sci. Technol. **18**(8), 2491 (2007).

20 January 2025 12:02:09

[22]R. de Kat and B. W. van Oudheusden, "Instantaneous planar pressure determination from PIV in turbulent flow," Exp. Fluids **52**, 1089–1106 (2012).

[23]B. W. Van Oudheusden, F. Scarano, E. W. M. Roosenboom et al., "Evaluation of integral forces and pressure fields from planar velocimetry data for incompressible and compressible flows," Exp. Fluids **43**, 153–162 (2007).

[24]J. Anderson, *Fundamentals of Aerodynamics* (McGraw hill, 2011).

[25]F. M. White and J. Majdalani, *Viscous Fluid Flow* (McGraw-Hill, New York, 2006).

[26]D. Ragni, A. Ashok, B. W. Van Oudheusden et al., "Surface pressure and aerodynamic loads determination of a transonic airfoil based on particle image velocimetry," Meas. Sci. Technol. **20**(7), 074005 (2009).

[27]D. Ragni, B. W. van Oudheusden, and F. Scarano, "Non-intrusive aerodynamic loads analysis of an aircraft propeller blade," Exp. Fluids **51**(2), 361–371 (2011).

[28]D. Ragni, B. W. van Oudheusden, and F. Scarano, "3D pressure imaging of an aircraft propeller blade-tip flow by phase-locked stereoscopic PIV," Exp. Fluids **52**(2), 463–477 (2012).

[29]P. L. van Gent, D. Michaelis, B. W. van Oudheusden et al., "Comparative assessment of pressure field reconstructions from particle image velocimetry measurements and Lagrangian particle tracking," Exp. Fluids **58**, 33 (2017).

[30]P. L. van Gent, F. F. J. Schrijer, and B. W. Van Oudheusden, "Assessment of the pseudo-tracking approach for the calculation of material acceleration and pressure fields from time-resolved PIV: Part I. Error propagation," Meas. Sci. Technol. **29**(4), 045204 (2018).

[31]P. L. van Gent, F. F. J. Schrijer, and B. W. Van Oudheusden, "Assessment of the pseudo-tracking approach for the calculation of material acceleration and pressure fields from time-resolved PIV: Part II. Spatio-temporal filtering," Meas. Sci. Technol. **29**(4), 045206 (2018).

[32]P. L. van Gent, B. W. van Oudheusden, and F. F. J. Schrijer, "Determination of mean pressure from PIV in compressible flows using the Reynolds-averaging approach," Exp. Fluids **59**, 41 (2018).

[33]B. W. van Oudheusden, "Principles and application of velocimetry-based planar pressure imaging in compressible flows with shocks," Exp. Fluids **45**(4), 657–674 (2008).

[34]J. D. Anderson, *Computational Fluid Dynamics: The Basics with Applications* (McGraw hill, 1995).

[35]S. Liu, J. Xu, and K. Yu, "MacCormack's technique-based pressure reconstruction approach for PIV data in compressible flows with shocks," Exp. Fluids **58**(6), 64 (2017).

[36]S. Liu, J. Xu, and K. Yu, "An iterative algorithm of pressure reconstruction from velocity data: Validation for different shock forms and flow velocity ranges," in Proceedings of the 18th International Symposium on Flow Visualization, Zurich, Switzerland, 2018.

[37]S. Liu, J. Xu, H. Gong et al., "Experimental comparison of PIV-based pressure measurements in supersonic flows with shock waves," Meas. Sci. Technol. **30**(10), 105201 (2019).

[38]S. Liu, J. Xu, H. Gong et al., "Assessment of streamline-based pressure reconstruction for PIV data in supersonic flows with shock waves," Exp. Fluids **61**(7), 161 (2020).

[39]S. Liu and J. Xu, "Assessment of pressure field and performance parameter reconstruction from velocity data for ramjet inlet," Aerosp. Sci. Technol. **110**, 106454 (2021).

[40]S. Liu, X.-R. Kong, J.-L. Xu et al., "Reconstruction measurement method for ramjet nozzle thrust based on PIV," J. Beijing Univ. Aeronaut. Astronaut. (published online 2023) (in Chinese).

[41]D. Ragni, F. Schrijer, B. W. Van Oudheusden et al., "Particle tracer response across shocks measured by PIV," Exp. Fluids **50**(1), 53–64 (2011).

[42]L. Laguarda, S. Hickel, F. F. J. Schrijer et al., "Shock-wave/turbulent boundary-layer interaction with a flexible panel," Phys. Fluids **36**(1), 016120 (2024).

[43]B. W. van Oudheusden, A. J. P. Jöbsis, F. Scarano et al., "Investigation of the unsteadiness of a shock-reflection interaction with time-resolved particle image velocimetry," Shock Waves **21**(5), 397–409 (2011).

[44]L. J. Souverein, B. W. Van Oudheusden, F. Scarano et al., "Application of a dual-plane particle image velocimetry (dual-PIV) technique for the unsteadiness characterization of a shock wave turbulent boundary layer interaction," Meas. Sci. Technol. **20**(7), 074003 (2009).

[45]A. Melling, "Tracer particles and seeding for particle image velocimetry," Meas. Sci. Technol. **8**(12), 1406 (1997).

[46]A. Schröder and C. E. Willert, *Particle Image Velocimetry: New Developments and Recent Applications* (Springer Science & Business Media, 2008).

[47]F. Scarano and B. W. Van Oudheusden, "Planar velocity measurements of a two-dimensional compressible wake," Exp. Fluids **34**(3), 430–441 (2003).

[48]R. A. Humble, F. Scarano, and B. W. Van Oudheusden, "Particle image velocimetry measurements of a shock wave/turbulent boundary layer interaction," Exp. Fluids **43**, 173–183 (2007).

[49]E. R. Van Driest, "The problem of aerodynamic heating," Aeronaut. Eng. Rev. **15**(10), 26–41 (1956).

[50]G. E. Elsinga, B. W. van Oudheusden, and F. Scarano, "Evaluation of aero-optical distortion effects in PIV," Exp. Fluids **39**, 246–256 (2005).

[51]P. L. Nel, A. M. Schreyer, F. F. J. Schrijer et al., "Highly separated transitional shock-wave/boundary-layer interactions: A spatial modal study," Phys. Fluids **36**(11), 116114 (2024).

[52]J. Erdos and A. Pallone, "Shock-boundary layer interaction and flow separation," in *Proceedings of the Heat Transfer and Fluid Mechanics Institute* (Stanford University Press, Stanford, CA, 1962), Vol. 15, pp. 239–254.

20 January 2025 12:02:09